Dynamic Study on the Fracture Interaction and the Predominant Frequency of the Induced Microseismic Signals during Hydraulic Fracturing

Zhenhua He* and **Benchun Duan**, Texas A&M University, College Station, USA

Abstract

Hydraulic fracturing has been used as a successful well stimulation method for decades. The created hydraulic fractures interact with the pre-existing fractures in a naturally fractured reservoir. Microseismicity is induced during the treatments. Microseismic monitoring has been a routine service to determine the geometry of the hydraulic fractures for over a decade. However, studies on the source mechanisms, the signal characteristics and predominant frequencies are still very limited, and many related problems remain ambiguous. Most of the current hydraulic fracturing models are based on a quasi-static framework. However, activation of the natural fractures and microseismicity generation and radiation during hydraulic fracturing are dynamic processes. We apply our in-house dynamic finite element geomechanics code to investigate these problems. First, the slip distributions and the ruptures along the activated natural fractures in the models with different cohesion are studied. We find that some activated natural fractures could have a partial failure while some others could fail entirely. The ruptures could be either unilateral or bilateral and the speeds may vary. The natural fractures and the hydraulic fracture can interact with each other. Different patterns of microseismic signals could be induced by different sources. Second, the effects of model parameters such as injection rate and Young's modulus on the predominant frequency of the microseismic signals are investigated. We find that injection rate doesn't affect the predominant frequencies much and a higher Young's modulus could shift the predominant frequencies to the high side. Rupture patterns (i.e., directionality and speed) along the natural fractures could affect the spectrum of the induced microseismic signals. The spectrum could either have multiple predominant frequencies or be relatively flat over the investigated frequency range.

Introduction

Hydraulic fracturing is a critical well stimulation technology for economically producing oil and gas from unconventional reservoirs (Warpinski et al. 2012). Natural fractures are present in most unconventional reservoirs and could affect the behaviors of the hydraulic fractures (Gale et al. 2007; Wu and Olson 2014). Extensive research including experimental (e.g., Blanton 1986; Warpinski and Teufel 1987; Renshaw and Pollard 1995; Beugelsdijk et al. 2000; Gu et al. 2011; Bahorich et al. 2012; Yang et al. 2016) and numerical (e.g., Zhang and Jeffrey 2006; Dahi-Taleghani and Olson 2011; Gu and Weng 2010; Olson and Wu 2012; Chuprakov et al. 2013; Wu and Olson 2014; Zhang et al. 2015; Duan 2016) work has been conducted to study the interaction between the natural and hydraulic fracturs. Akulich and Zvyagin (2008) and Duan (2016) presented that the activation of the natural fractures could change the opening profile of the hydraulic fracture. When the fracturing fluid pressure within a hydraulic fracture accumulates and the effective

---

DOI: 10.14800/IOGR.428

Received June 29, 2018; revised July 19, 2018; accepted July 26, 2018.

*Corresponding author: happidence1@tamu.edu

normal stress reached the rock tensile strength, the rock breaks and abrupt or jerky opening (Hu et al. 2017) occurs. Most of these studies are based on a quasi-static framework, while abrupt opening and unstable shear slip of fractures are dynamic processes. In this study, we investigate dynamic interactions between a hydraulic fracture and pre-existing nature fractures.

When a hydraulic fracture is propagating in a naturally fractured reservoir, seismicity could be induced. Warpinski et al. (2012) studied the induced seismicity in many fracturing treatments in all the major shale basins in North America and found the magnitudes are very small (i.e., -3.0 M_w ~ 1.0 M_w and typically around -2.5 M_w). So, the induced events are called microseismic events. Warpinski et al. (2013) also pointed out the source mechanisms of the microseismicity still remains ambiguous. Zeng et al. (2014) presented that the opening and growth of tensile fractures and shear slip along fractures during hydraulic fracturing are the major source mechanisms for the induced microseismic events and showed microseismic traces recorded on six stations. And these traces include some specific patterns of signals such as isolated spiky signals and continuous signals with coda waves. Similar patterns of microseismic signals can also be found in Song et al. (2010). Duan (2016) numerically studied and also presented such characteristics of the induced microseismic signals from different sources. Different sensors are used to record the microseismic signals in the petroleum industry. Warpinski (2009) stated that the best sensors used to acquire the microseismic data will be those with high sensitivity, low self-generated noise and a flat response over the frequency range of interest. In microseismic monitoring, there are two main types of sensors: 'omni-geophone' and 'GAC' (Geophone Accelerometer) sensor. An omni-geophone can be placed in any orientation and a GAC sensor can provide acceleration data. Geophones measure velocity and accelerometers measure acceleration. However, they respond well to different ranges of frequency (Warpinski 2009). Determination of predominant frequencies could be helpful for sensor selection (Maxwell, 2014). In this study, we investigate whether some model parameters such as the rock properties and injection parameters could affect the predominant frequencies of microseismic signals.

Model And Methods

Figure 1 shows the model setup. There is one hydraulic fracture (HF) and one set of inclined natural fractures (NFs) in the model. This set of NFs includes eight uniformly distributed NFs. Their length is about 58 meters and spacing is about 35 meters. The red triangles in the model indicate the location of the receivers. The parameters are listed in Table 1. The reservoir is assumed to be at around 2500 meters in depth. The maximum and minimum horizontal stresses and initial reservoir pore pressure are 55, 40 and 25 MPa, respectively. Based on the data from Stanford Rock Physics Laboratory (i.e., Mavko, 2005), the rock property values are selected. Kohli and Zoback (2013) presented that some shale samples show frictional coefficients around 0.4. The fracturing fluid with a viscosity of 0.02 Pa · s is injected at a rate of 0.053 m^3/s (i.e., about 20 bpm).

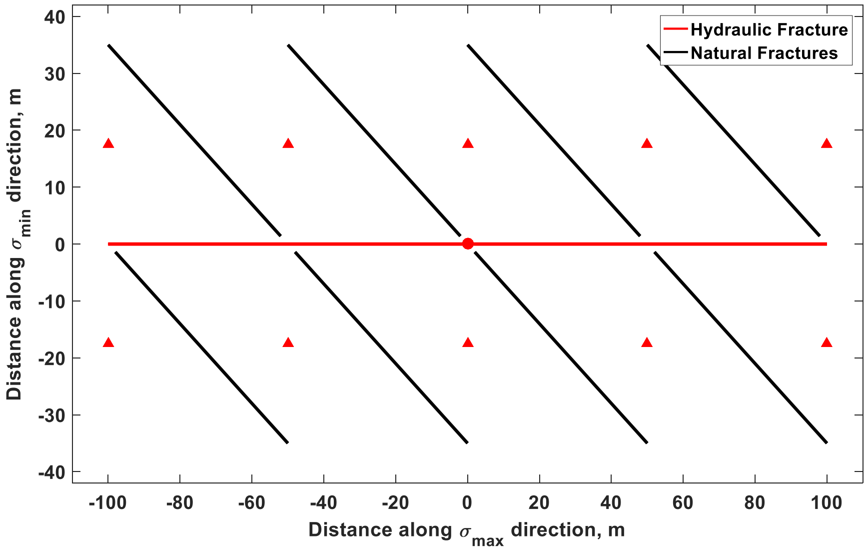

Figure 1—Model setup.

Table 1—Model parameters.

Parameters	Model A	Model B (Base model)	Model C
Density ρ (kg/m^3)	2400		
Young's modulus E (GPa)	10.0		
Poisson's ratio ν	0.2		
P wave velocity V_p (m/s)	2200		
S wave velocity V_s (m/s)	1300		
Static friction μ_s	0.35		
Dynamic friction μ_d	0.25		
Critical slip distance d_0 (m)	0.001		
Cohesion c_o (MPa)	1.05	0.35	0.70
Skempton's coefficient B	0.8		
Tensile strength T (MPa)	1		
Initial σ_{xx} (MPa)	55		
Initial σ_{yy} (MPa)	40		
Initial σ_{xy} (MPa)	0		
Initial pore pressure p (MPa)	25		
Injection fluid viscosity η (Pa · s)	0.02		
Hydraulic fracture height h_f (m)	50.0		
Injection rate i (m^3/s)	0.053		

In this study, a dynamic finite element method (Duan 2016) is applied to perform numerical simulations. EQdynaFrac is developed from another dynamic FEM code EQdyna (Duan and Oglesby 2006; Duan and Day 2008; Duan 2010; Duan 2012) for rupture dynamics and seismic wave propagation. EQdyna follows the standard procedure of FEM (e.g. Hughes 2000) to solve a dynamic problem and has been verified on many benchmark problem (Harris et al. 2009;2011;2018).

The dynamic FEM solves the equations of motions as below.

$$div(\boldsymbol{\sigma}) + \rho \mathbf{b} = \rho \dot{\boldsymbol{v}}, \dots\dots(1)$$

where, $\boldsymbol{\sigma}$ is the stress tensor, ρ is density, **b** is body force vector and $\dot{\boldsymbol{v}}$ is the acceleration vector.

In the models, EQdynaFrac treats fractures as surfaces across which a discontinuity in the displacement vector is permitted. On a fracture, one FEM node is split into two halves and the two halves interact with each other by the traction acting on the surface between them.

Hydraulic fracturing opening and propagation are the source of deformation in each model. The hydraulic fracturing propagation and fracturing net pressure follows the non-leak off PKN model (Valko and Economides 1995). The equations are as below,

$$l_f(t) = \left(\frac{625}{512\pi^3}\right)^{\frac{1}{5}} \left(\frac{i^3 E'}{\eta h_f^4}\right)^{\frac{1}{5}} t^{\frac{4}{5}}, \dots\dots(2)$$

$$p_n(x,t) = \left(\frac{32\eta i}{\pi}\right)^{\frac{1}{4}} \frac{E'^{\frac{3}{4}}}{h_f} \left(l_f(t) - |x|^{\frac{1}{4}}\right)^{\frac{1}{4}}, |x| \le l_f(t), \dots\dots(3)$$

where i is the injection rate, E' is the plane strain modulus and calculated as $E'=E/(1-v_2)$, E is the Young's modulus, v is the Poisson ratio, η is the fluid viscosity, and h_f is the fracture height. The injection well is assumed at the origin point in Figure 1.

The Coulomb failure criterion and a linear slip-weakening law (e.g., Andrews 1976) which is widely used in the earthquake community control the shear failure along the fractures. The two equations are as below.

$$\tau_c = \mu(\sigma_n - p) + c, \quad (4)$$

$$\mu(l) = \begin{cases} \mu_s - (\mu_s - \mu_d) \times \frac{l}{d_0} & when\ l \leq d_0 \\ \mu_d & when\ l > d_0 \end{cases}, \quad (5)$$

where τ_c is the shear strength, μ is the frictional coefficient, c is cohesion, σ_n is the normal stress, and p is the pore pressure, l is the slip distance, μ_s and μ_d are static and dynamic frictional coefficients, respectively, and d_0 is the critical slip distance. So, $(\sigma_n - p)$ is the effective normal stress.

When the effective normal stress along a fracture reaches the rock tensile strength, the fracture opens. The friction disappears, and the tensile strength becomes zero where the fracture opens. The two walls are regulated not to interpenetrate each other.

We assume the medium in the models is undrained, fluid saturated and linearly elastic. The pore pressure is time-dependent. According to Harris and Day (1993), its increment is a function of the Skempton coefficient B, undrained Poisson ratio υ, and the time dependent normal stress changes in the x- and y-directions $\Delta\sigma_{xx}(\mathrm{t})$ and $\Delta\sigma_{yy}(\mathrm{t})$. The equation is shown below.

$$\Delta \mathrm{p}(\mathrm{t}) = -\mathrm{B}[(1 + \upsilon)/3][\Delta\sigma_{xx}(\mathrm{t}) + \Delta\sigma_{yy}(\mathrm{t})] \quad (6)$$

In our models, the main model region (i.e., Figure 1) that includes all fractures is at the center. A buffer region surrounding the main model region is set to prevent the reflections at the model boundaries from traveling back to the main model region.

Results And Analysis

Activation of the NFs in Different Models. When the HF is propagating in the model, the induced stress perturbations could activate some of the NFs. The activation of the NFs of the three models (i.e., Models A, B and C in Table 1) is shown in **Figure 2**. In Model A, the cohesion of the NFs is the largest and we can see no NFs are activated. Model B has a much smaller cohesion (i.e., 0.35 MPa), and all the NFs are activated along the whole length. Model C has a little larger cohesion (i.e., 0.7 MPa) than Model B, and only some of the NFs are activated. We can see the lower (i.e., the region with negative y values in Figure 1) fourth (counted from left to right) and the upper first NFs are entirely activated, and the lower second and the upper third NFs are partially activated although the slip magnitudes are very small comparatively (i.e., the inset plots in Figure 2).

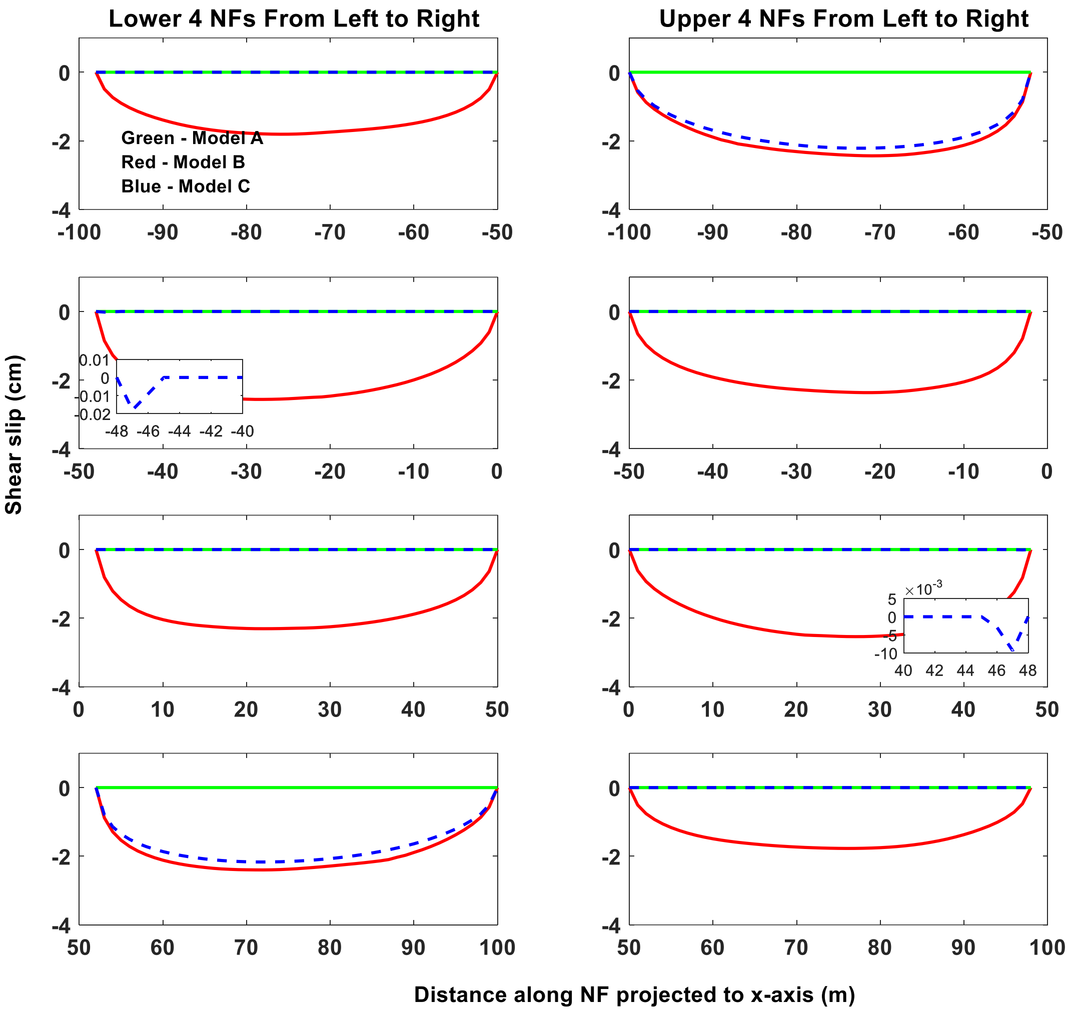

Figure 2—Activation of the NFs in the Models A, B and C.

Displacement Profiles along the HF in Different Models. In **Figure 3**, the top panel (a) shows the displacement profile of the two HF walls in the three models, the middle panel (b) shows the width profile along the HF, and the bottom panel (c) shows the shearing profile (i.e., the relative displacement of the two walls in the shear direction) along the HF. In Model A, there are no NFs activated as shown in Figure 2, and the two HF walls open in the opposite directions. The open width profile is almost elliptical as shown in Figure 3(b) and there is no shearing between the two walls as shown in Figure 3(c). In Model B, all the NFs are activated. The displacement profiles of the two HF walls are greatly distorted. The flow channel along this HF is very tortuous. In Figure 3(b), the width profile has three peaks at x = -50, 0 and 50 meters corresponding to the effect of the slip of the NFs intercepting x-axis at x = -50, 0 and 50 meters. From Figure 3(b), we can see that the HF only propagates to 80 meters. So, the other two NFs intercepting x-axis at -100 and 100 meters do not have much impact on the width profile. Figure 3(c) shows there is shearing along the HF. In Model C, the lower fourth and upper first NFs are entirely activated, and the lower second and upper third NFs are partially activated with very small slip at one end respectively. In Figure 3(b), the width profile has significant change at x = -50 and 50 meters corresponding to the effect of the activated NFs intercepting x-axis at -50 and 50 meters. Also, there is shearing along the HF, and different senses of shear can occur.

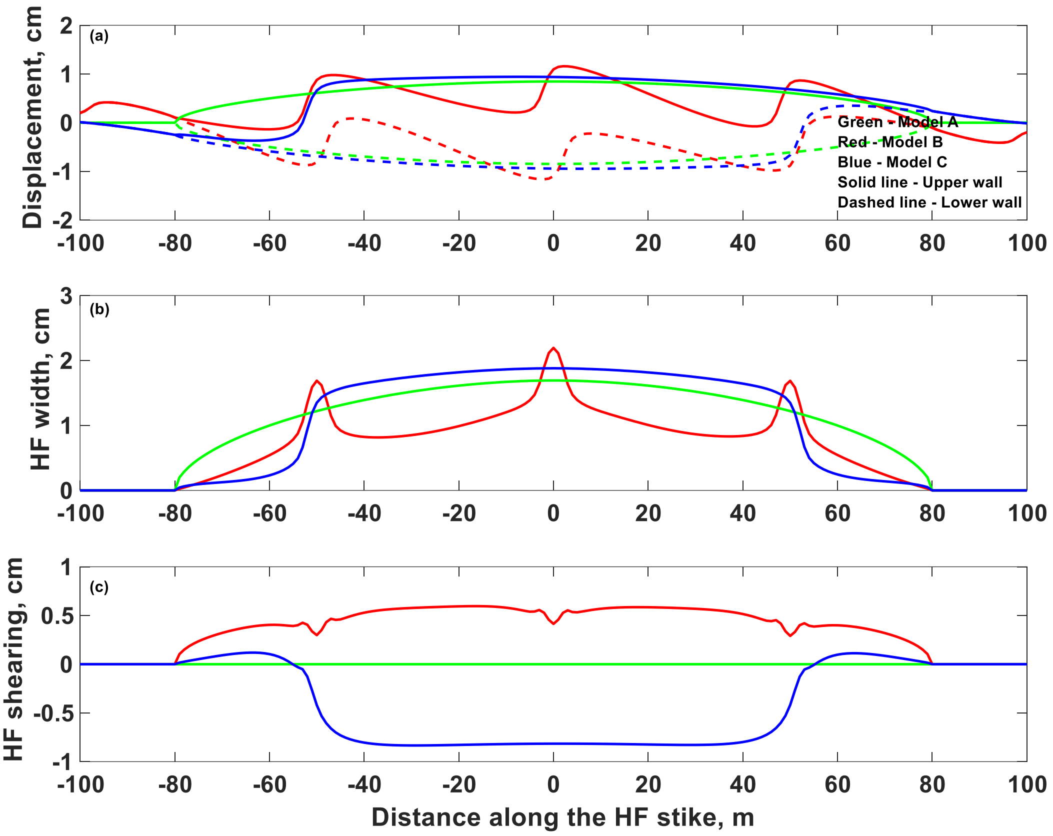

Figure 3—The top panel shows the displacements of the two HF walls in the three models; The middle panel shows the width profile along the HF; And the bottom panel shows the shearing profile along the HF.

Figure 4 shows the evolution of the HF width at the wellbore in the three models. In Model A, no NFs are activated. There is no interaction between HF and NFs and thus no abrupt change in the width. However, Models B and C have abrupt/jerky opening during the hydraulic fracturing process. The abrupt opening occurs at around 98 seconds in Model B and 163 seconds in Model C and are caused by the interaction between the HF and the activated NFs. After this abrupt opening, the HF width gradually gets back to the normal trend (i.e., green line in Figure 4). By looking at the curve of the HF width evolution more closely (i.e., the inset plot of Figure 4), the HF has closing and opening motions.

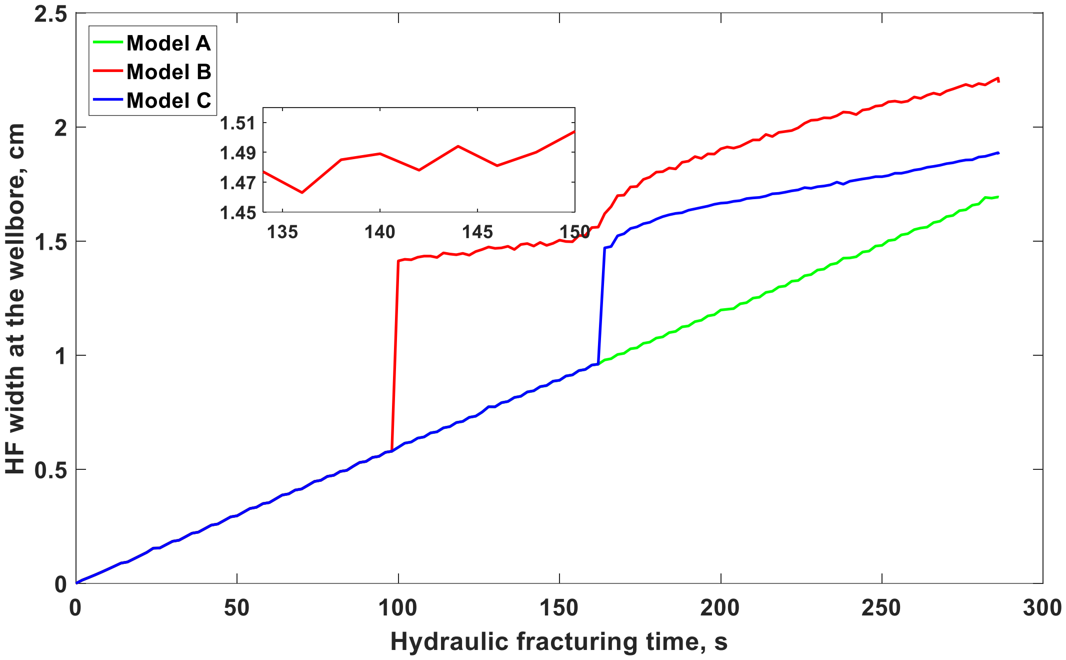

Figure 4—Evolution of the HF width at the wellbore in the three models.

Rupture along the NFs in Different Models. The rupture along the NFs in Models B and C are shown in **Figures 5** and **6**, respectively. From Figure 5, we can see that the NFs are activated and slide at around 98 seconds, which is corresponding to the time when the abrupt opening of the HF at the wellbore occurs. The patterns of the rupture (i.e., rupture directionality and speed) along the NFs could be very different. The ruptures could be unilateral (i.e., Figures 5(a) and 5(h)) and bilateral (i.e., Figures 5(b), 5(c), 5(d), 5(e), 5(f) and 5(g)). The rupture speeds in the Figures 5(a) and 5(h) are almost constant along the NFs and they are 2173 m/s and 2157m/s, respectively. The speeds of the other ruptures vary along the NFs. We take Figures 5(c) and 5(f) for examples. Both the ruptures initiate from an inner location on the NFs and then propagate bilaterally to the two ends. From the initiation point to the two ends, the rupture starts from a very slow speed and then gradually accelerates to a high speed respectively. In Figure 6, there are some blank plots (i.e., Figures 6(b), 6(d), 6(e) and 6(g)), which indicate that the NFs are not activated. By looking at the Figures 2 and 6 together, we can see that the ruptures in Figures 6(a) and 6(h) are large while the ruptures in Figures 6(c) and 6(f) are very small and would not affect the HF opening much. Therefore, the abrupt opening of the HF in Model C shown in Figure 4 is caused by the activation of the upper first (i.e., Figure 6(a)) and lower fourth (i.e., Figure 6(h)) NFs. The activation of these two NFs occurs around 163 seconds, which is corresponding to the time when the abrupt opening of the HF happens.

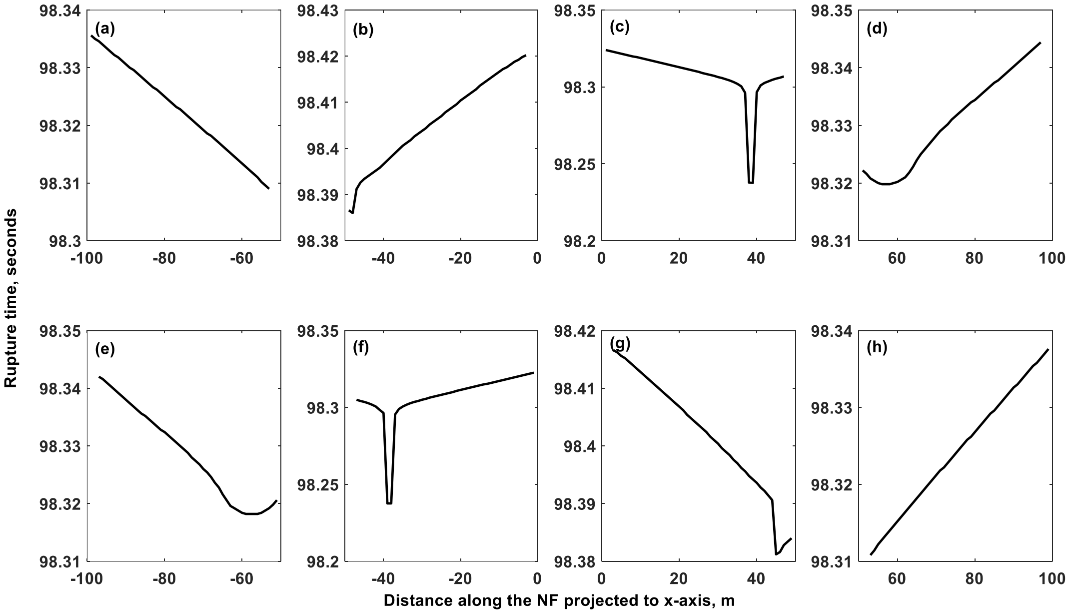

Figure 5—Rupture along the NFs in Model B (i.e., cohesion = 0.35 MPa).

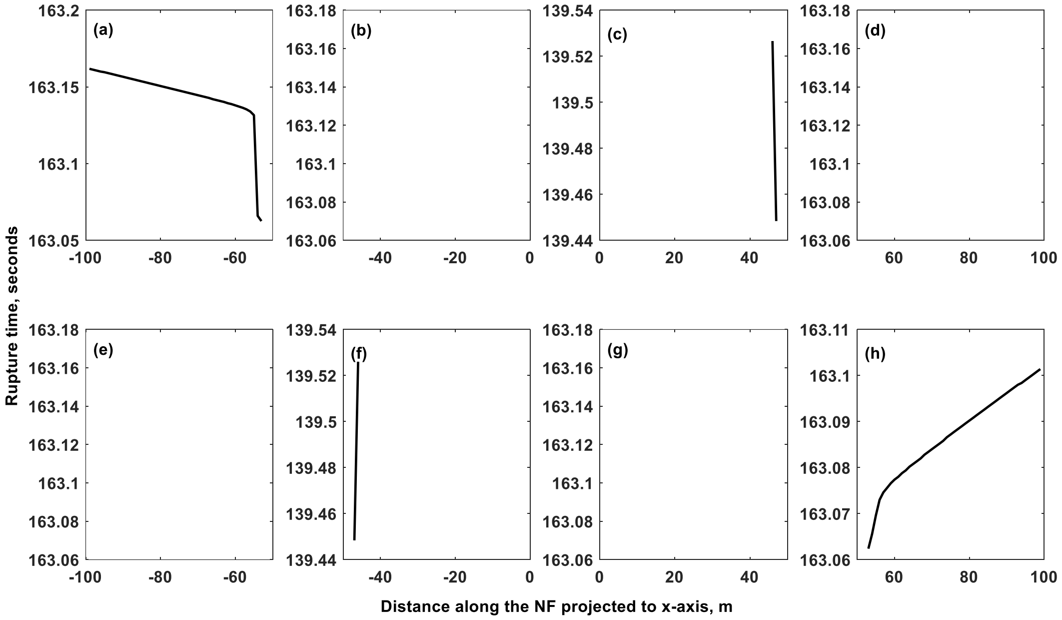

Figure 6—Rupture along the NFs in Model C (i.e., cohesion = 0.7 MPa).

Induced Microseismicity in Different Models. The x- and y- components of the seismogram of the induced microseismicity during hydraulic fracturing in Models A, B and C are shown in **Figures 7** and **8**, respectively. In Model A, there are no NFs activated. So, the only source of the microseismic signals is the non-smooth opening (e.g., the slightly wiggly opening profile in Figure 4) of the HF as suggested by Duan (2016). Isolated spiky signals are generated in both x- and y- components and they are seismic signals with very short rise time as shown in the inset plot of Figure 7. Therefore, these isolated spiky signals are induced by HF non-smooth opening, as proposed by Duan (2016). In Model B, there are NFs activated at around 98 seconds. Comparing the Models A and B in Figures 7 and 8, the microseismic signals are the same from 0-98 seconds. When the NFs are activated at about 98 seconds, continuous signals with relatively large amplitude and long-duration and low-amplitude coda waves are generated. These signals are caused by the unstable shear sliding along the NFs as presented in Duan (2016). This is similar in Model C when the NFs are activated at around 163 seconds.

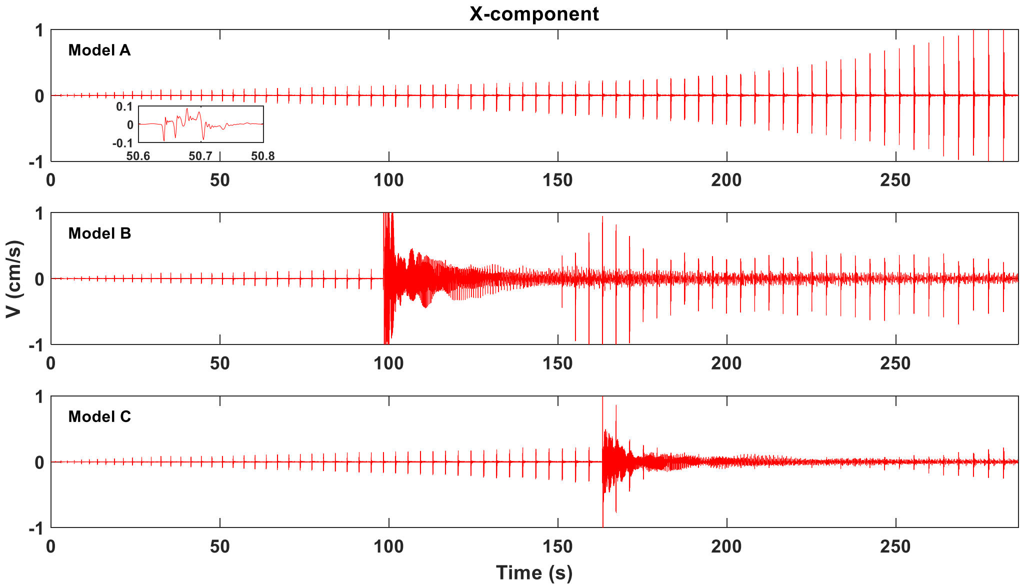

Figure 7—The x-component of the induced microseismicity during hydraulic fracturing. The seismic signals are obtained from the lower first receiver, whose location is shown in Figure 1.

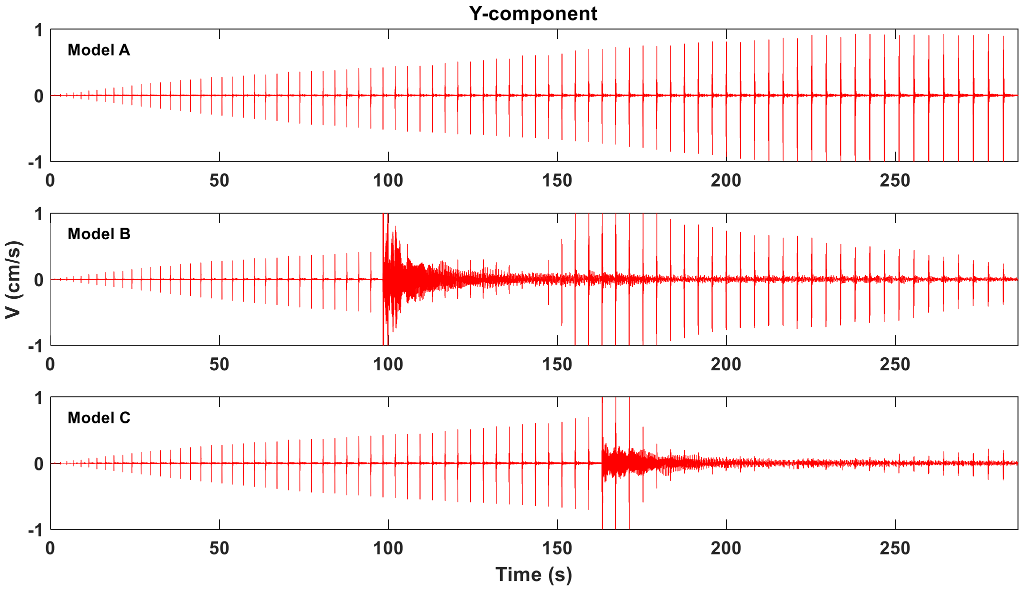

Figure 8—The y-component of the induced microseismicity during hydraulic fracturing. The seismic signals are obtained from the lower first receiver, whose location is shown in Figure 1.

Predominant Frequency of the Induced Microseismicity. To eliminate the impact of the activation of other NFs on the microseismic signals, in this section we keep only one NF in each model. **Figure 9** shows the model configurations with only one NF. In the left plot (i.e., L1 model), only the lower first (L1) NF exists. The black solid line indicates the location of the NF. The black dashed lines indicate the locations of the other NFs in the previous models, but they do not exist in this model. In the right plot (i.e., L4 model), only the lower fourth (L4) NF exists.

In these models, the element length in the x-direction is 1 meter. Six elements are used to represent a full wavelength. So, the highest frequency that can be resolved is $f_{max} = \frac{V_s}{6\times dx} = \frac{1300}{6\times 1} = 216.6\ (Hz)$.

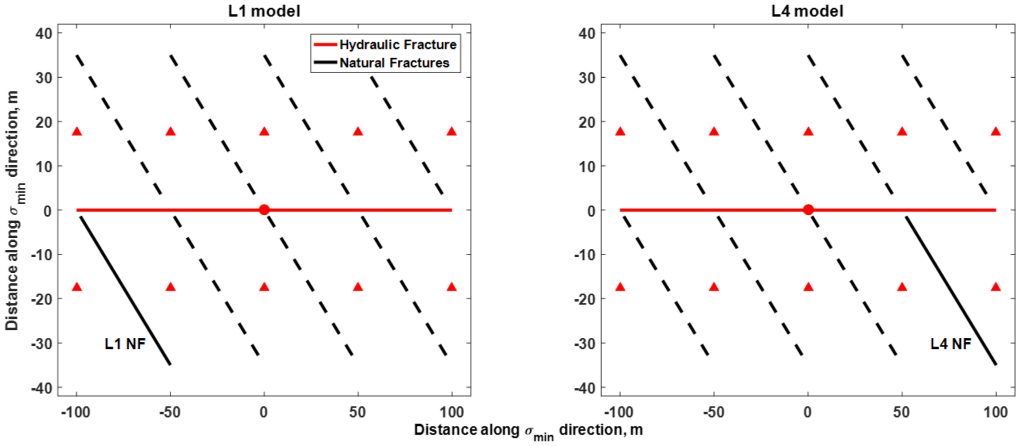

Figure 9—Model setup with only one NF.

The seismogram of the induced microseismicity, the spectrum and the rupture along the NFs in these two models are studied and shown in **Figure 10**. The top half is for L1 model. In the subplot L1(a), we can see that a continuous signal with a coda wave starts to occur around 212 seconds. There are multiple distinct predominant frequencies of 17 Hz, 100 Hz, and 170 Hz as shown in the subplot L1(b). The subplot L1(c) shows the rupture along the NF. It initiates around the center and then propagates bilaterally to the left and right sides. The speed varies along each rupture path. The bottom half is for L4 model. A continuous signal appears at about 155 seconds (i.e., subplot L4(a)). Its spectrum is relatively flat over the frequency range. The predominant frequencies are not distinct, and the spectrum mainly lies in the high frequency band. The subplot L4(c) shows that the rupture initiates from the left end, and then propagates unilaterally to the right end. The speed varies at the beginning and then remains almost a constant afterwards.

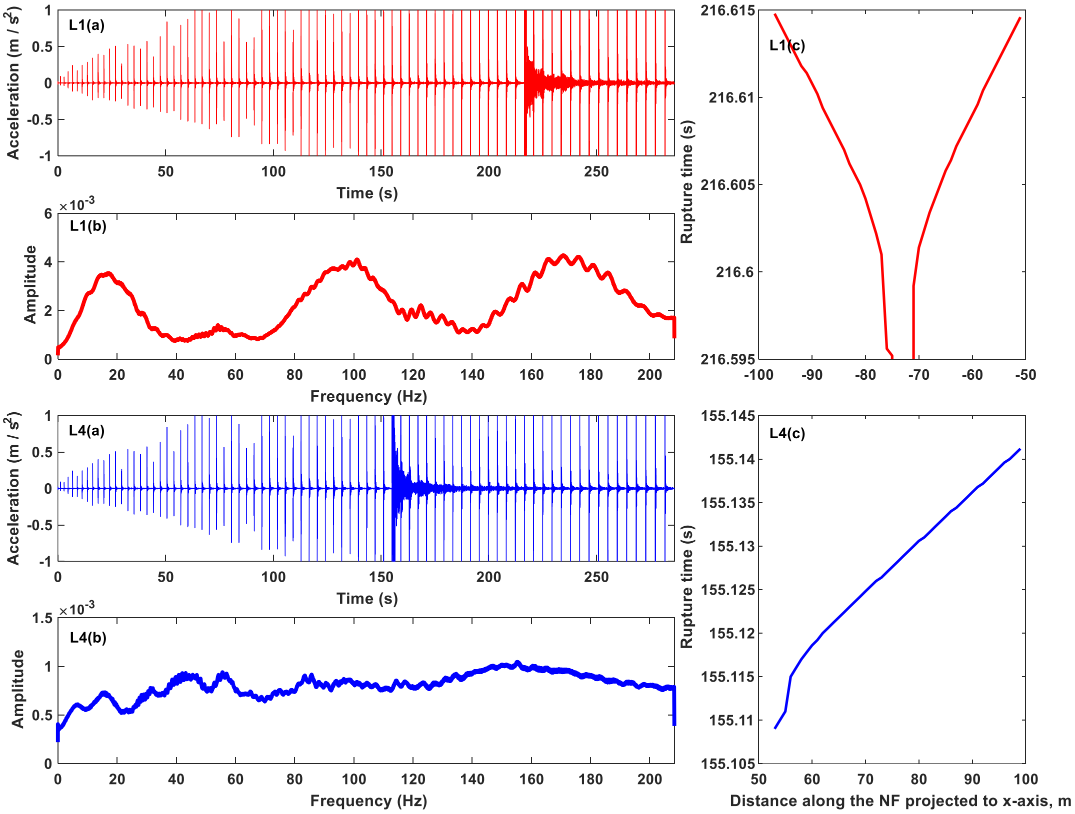

Figure 10—The x-component of the seismogram of the induced microseismicity, the spectrum and the rupture along the NFs in the two different models (i.e., L1 and L4). The top half is for the model with only the lower first (i.e., L1) NF, and the bottom half is for the model with only the lower fourth (i.e., L4) NF.

Effect of Injection Rate on the Predominant Frequency. The effect of injection rate on the predominant frequency is studied. The L1 and L4 model configurations are also used in this section. The base model parameters are shown in Table 1 (i.e., the base model column). For each model configuration, the injection rate is varied in three different cases. The injection rates in the other two cases double and triple the injection rate in the base case, respectively. At the end of the simulation, the hydraulic fractures propagate to the same length in all three cases.

Figure 11 presents the spectrums of the induced microseismicity in the three cases under L1 and L4 model configurations, respectively. The top panel shows the spectrums in L1 model configuration. We can see that there are three distinct predominant frequencies in each of the three cases and the three predominant frequencies in one case are very close to those in the other two cases correspondingly. However, the amplitudes in the higher-injection-rate case are greater than those in the lower-injection-rate case. The bottom panel shows the spectrums in L4 model configuration. In general, the spectrums are all relatively flat and mainly lie in the high frequency band. The predominant frequencies of the three cases are all around 150 Hz. The amplitude also increases with injection rate.

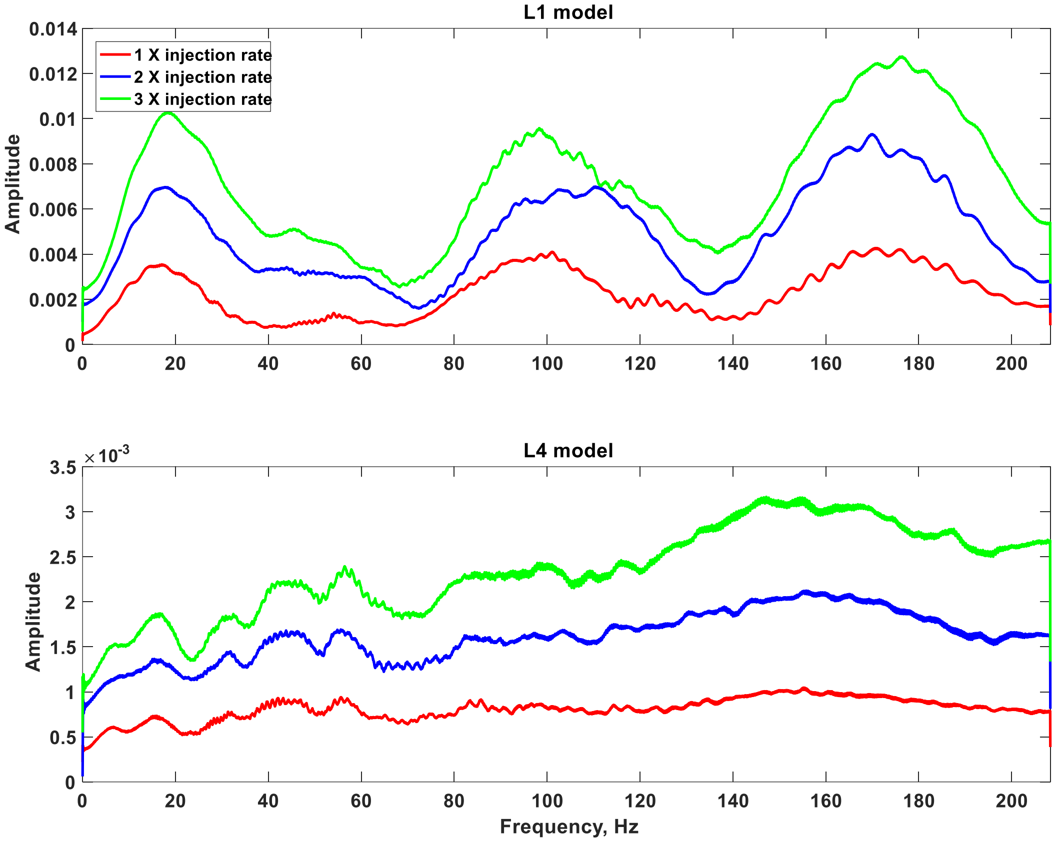

Figure 11—Comparison of the spectrums of the microseismicity induced in the models with different injection rates.

Effect of Young's Modulus on the Predominant Frequency. We also investigate the effect of Young's modulus on the predominant frequency and make use of the L1 and L4 model configurations in this section. The base model parameters are also as in Table 1 (i.e., the base model column). For each model configuration, the Young's modulus is varied in three different cases and are 10.0, 10.8, 11.6 GPa, respectively. At the end of the simulation, the hydraulic fractures propagate to the same length in all three cases.

The spectrums of the induced microseismicity in the three cases under L1 and L4 model configurations respectively are shown in **Figure 12**. The top panel shows the spectrums in L1 model configuration. For each spectrum, there are multiple distinct predominant frequencies. Comparing different cases and the second predominant frequency, we can see the predominant frequency shifts to the right (i.e., high frequency) when the Young's modulus increases. The spectrums in L4 model configuration are shown in the bottom panel. All the spectrums are relatively flat over the investigated frequency range and it is hard to distinguish the change or shift of the predominant frequencies with the Young's modulus.

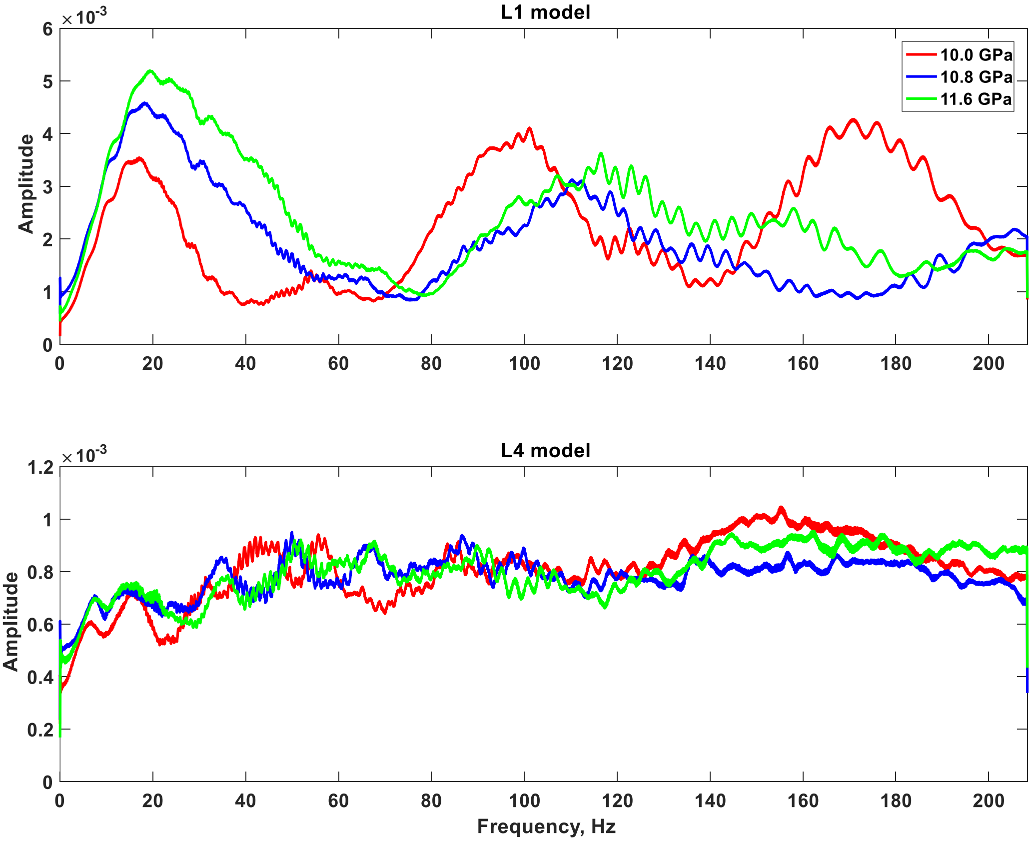

Figure 12—Comparison of the spectrums of the microseismicity induced in the models with different Young's modulus.

In summary, from the study on the effects of injection rate and Young's modulus on the predominant frequency of the induced microseismicity, we can see that the spectrum could either have multiple distinct predominant frequencies or could be relatively flat over the investigated frequency range. The injection rate doesn't affect the predominant frequencies much, however, a higher Young's modulus could shift the predominant frequency to the high side.

Discussion

During hydraulic fracturing, the activation of NFs and the associated microseismic generation and radiation are dynamic processes. Dynamic modeling is needed to accurately model the fracture interaction and induced microseismicity. In this study, we do not attempt to simulate the fluid flow in a hydraulic fracture. The well-known non-leak-off PKN model is implemented. Although the models may lack of acute fluid pressure response when the hydraulic fracture has sudden opening and/or closing, they still capture the main characteristics of all the processes associated with hydraulic fracturing.

In our models, some frequency spectrums have multiple distinct predominant frequencies (e.g., L1(b) in Figure 10) and others could be relatively flat over the investigated frequency range (e.g., L4(b) in Figure 10). Maxwell and Cipolla (2011) presented similar frequency spectra of microseismic events induced by hydraulic fracturing. For natural earthquakes, Martin (2016) proposed that the controlling factors of the frequency are the size, geometry and the rupture pattern of the earthquake source. We also studied the rupture patterns in our models and found that rupture directionality could affect the frequency spectrum. Bilateral ruptures may induce multiple predominant frequencies, while unliteral ruptures may induce relatively fat frequency spectrums.

Effect of Young’s modulus on the predominant frequency is studied. Young’s modulus is not a direct input parameter in our dynamic models while P and S wave velocities, V_p, V_s are. Mavko (2005) in Stanford rock physics lab presented a saturated shale rock (Pore pressure, P_p around 25 MPa) has V_s of 1300-1500 m/s under the confining pressure of 40-55 MPa. In these studies, varying Young’s modulus is achieved by varying V_p and V_s and V_p/V_s is assumed to be about 1.7 for the rocks.

Conclusions

We apply our in-house finite element geomechanics code to study the fracture interaction and the predominant frequency of the induced microseismic signals. Some conclusions are achieved as below.

1. Cohesion affects the activation of the NFs during hydraulic fracturing process. The NFs are easier to be activated in the low-cohesion models. The NFs could be activated to different extents. Some NFs may slide along the whole lengths, while some others may slide along just part of the whole lengths.
2. The opening of the HF could be affected by the activation of the NFs, which changes the width profile along the HF. Abrupt opening or closing (i.e., increase or decrease in HF width) could occur when NFs are activated.
3. When a NF is activated, the rupture could be unilateral or bilateral along the NF. The speed of the rupture could be constant or varying along the path.
4. Rupture patterns (i.e., directionality and speed) along the NFs could affect the spectrum of the induced microseismicity. The spectrum could have multiple predominant frequencies or could be relatively flat over the investigated frequency range.
5. Injection rate doesn’t affect the predominant frequencies much. A higher Young’s modulus could shift the predominant frequency to the high side.

Acknowledgement

We appreciate the funding support from The Crisman Institute and The Berg-Hughes Center at Texas A&M University.

Conflicts of Interest

The author(s) declare that they have no conflicting interests.

References

Akulich, A. and Zvyagin, A. 2008. Interaction between Hydraulic and Natural Fractures. *Fluid dynamics* **43**(3): 428-435.

Andrews, D. 1976. Rupture Velocity of Plane Strain Shear Cracks. *Journal of Geophysical Research* **81**(32): 5679-5687.

Bahorich, B., Olson, J. E., and Holder, J. 2012. Examining the Effect of Cemented Natural Fractures on Hydraulic Fracture Propagation in Hydrostone Block Experiments. Paper presented at SPE Annual Technical Conference and Exhibition, San Antonio, Texas, 8-10 October. SPE-160197-MS.

Beugelsdijk, L., De Pater, C., and Sato, K. 2000. Experimental Hydraulic Fracture Propagation in A Multi-Fractured Medium. Paper presented at SPE Asia Pacific conference on integrated modelling for asset management, Yokohama, Japan, 25–26 April. SPE-59419-MS.

Blanton, T.L. 1986. Propagation of Hydraulically and Dynamically Induced Fractures in Naturally Fractured Reservoirs. Paper presented at SPE unconventional gas technology symposium, Louisville, Kentucky, 18-21 May. SPE-15261-MS.

Chuprakov, D., Melchaeva, O., and Prioul, R. 2013. Hydraulic Fracture Propagation across a Weak Discontinuity Controlled by Fluid Injection. Paper presented at ISRM International Conference for Effective and Sustainable Hydraulic Fracturing, Brisbane, Australia, 20-22 May. ISRM-ICHF-2013-008.

Dahi-Taleghani, A. and Olson, J. E. 2011. Numerical Modeling of Multistranded-Hydraulic-Fracture Propagation: Accounting for the Interaction between Induced and Natural Fractures. *SPE Journal* **16**(3): 575-581.

Duan, B. 2016. Spontaneous Rupture on Natural Fractures and Seismic Radiation during Hydraulic Fracturing Treatments. *Geophysical Research Letters* **43**(14): 7451-7458.

Duan, B. 2010. Role of Initial Stress Rotations in Rupture Dynamics and Ground Motion: A Case Study with Implications for the Wenchuan Earthquake. *J. Geophys. Res.* **115**(3):34-50.

Duan, B. and Day, S. M. 2008. Inelastic Strain Distribution and Seismic Radiation from Rupture of a Fault Kink. *J. Geophys. Res.* **113**(5):23-31.

Gale, J. F., Reed, R. M., and Holder, J. 2007. Natural Fractures in the Barnett Shale and their Importance for Hydraulic Fracture Treatments. *AAPG bulletin* **91**(4): 603-622.

Gu, H. and Weng, X. 2010. Criterion for Fractures Crossing Frictional Interfaces at Non-Orthogonal Angles. Paper presented at 44th US rock mechanics symposium and 5th US-Canada rock mechanics symposium, Salt Lake City, Utah, 27–30 June. ARMA-10-198.

Harris, R. A. and Day S. M. 1993. Dynamics of Fault Interaction: Parallel Strike‐Slip Faults. *Journal of Geophysical Research: Solid Earth* **98**(3): 4461-4472.

Harris, R. A., Barall, M., Archuleta, R., et al. 2009. The SCEC/USGS dynamic Earthquake Rupture Code Verification Exercise. *Seismol. Res. Lett.* **80**(1):119–126.

Harris, R. A., Barall, M., Aagaard, B. et al. 2011. Verifying a Computational Method for Predicting Extreme Ground Motion *Seismol. Res. Lett.* **82**(5):638-644.

Hu, H., Li, A., and Zavala‐Torres, R. 2017. Long‐period Long‐duration Seismic Events During Hydraulic Fracturing: Implications for Tensile Fracture Development. *Geophysical Research Letters* **44**(10): 4814-4819.

Hughes, T.J.R. 2000. The Finite Element Method: Linear Static and Dynamic Finite Element Analysis. Dover, Mineola, New York.

Kohli, A. H. and Zoback, M. D. 2013. Frictional Properties of Shale Reservoir Rocks. *Journal of Geophysical Research: Solid Earth* **118**(9): 5109-5125.

Martin, K. 2016. Seismology: What is the Frequency in HZ of an Earthquake's P-wave? Retrieved from https://www.quora.com/Seismology-What-is-the-frequency-in-Hz-of-an-earthquakes-p-wave.

Mavko, G. 2005. Conceptual Overview of Rock and Fluid Factors That Impact Seismic Velocity and Impedance. *Solid Earth* **3**(2)32-45:

Maxwell, S. 2014. Microseismic Imaging of Hydraulic Fracturing: Improved Engineering of Unconventional Shale Reservoirs. *Microseismic Acquisition and Survey Design* **8**(3):31-52.

Maxwell, S. C. and Cipolla, C. L. 2011. What Does Microseismicity Tell Us About Hydraulic Fracturing? Paper presented at SPE Annual Technical Conference and Exhibition, Denver, Colorado, USA, 30 October–2 November. SPE-146932-MS.

Olson, J. E. and Wu, K. 2012. Sequential vs. simultaneous Multizone Fracturing in Horizontal Wells: Insights from A Non-Planar, Multifrac Numerical Model. Paper presented at SPE Hydraulic Fracturing Technology Conference, The Woodlands, Texas, USA, 6–8 February. SPE-152602-MS.

Renshaw, C. and Pollard, D. 1995. An Experimentally Verified Criterion for Propagation Across Unbounded Frictional Interfaces in Brittle, Linear Elastic Materials. *International journal of rock mechanics and mining sciences & geomechanics abstracts* **32**(3): 237-249.

Song, F., Kuleli, H. S., Toksoz, M. N., et al. 2010. An improved Method for Hydrofracture-Induced Microseismic Event Detection and Phase Picking. *Geophysics* **75**(6): 47-52.

Valko, P. and Economides, M. J. 1995. *Hydraulic Fracture Mechanics*. Chichester, UK: Wiley.

Warpinski, N. R., Mayerhofer, M., Agarwal, K., et al. 2013. Hydraulic-fracture Geomechanics and Microseismic-Source Mechanisms. *SPE Journal* **18**(4): 766-780.

Warpinski, N. R., Du, J., and Zimmer, U. 2012. Measurements of Hydraulic-Fracture-Induced Seismicity in Gas Shales. *SPE Production & Operations* **27**(3): 240-252.

Warpinski, N. 2009. Microseismic Monitoring: Inside and Out. *Journal of Petroleum Technology* **61**(11): 80-85.

Warpinski, N. and Teufel L. 1987. Influence of Geologic Discontinuities on Hydraulic Fracture Propagation (includes associated papers 17011 and 17074). *Journal of Petroleum Technology* **39**(2): 209-220.

Wu, K. and Olson J. E. 2014. Mechanics Analysis of Interaction Between Hydraulic and Natural Fractures in Shale Reservoirs. Paper presented at Unconventional Resources Technology Conference (URTEC), Denver, Colorado, USA, 25-27 August. URTec-1922946.

Yang, X., Burghardt, J., Zhang, H., et al. 2016. Experimental Study of Hydraulic Fracture/Natural Fracture Interaction on a Tight Sandstone Formation. Paper presented at Unconventional Resources Technology Conference (URTEC), San Antonio, Texas, USA, 1-3 August. URTec-2460449.

Zeng, X., Zhang, H., Zhang, X., et al. 2014. Surface Microseismic Monitoring of Hydraulic Fracturing of a Shale-Gas Reservoir Using Short-Period and Broadband Seismic Sensors. *Seismological Research Letters* **85**(3): 668-677.

Zhang, F., Qiu, K., Yang, X., et al. 2015. A Study of the Interaction Mechanism between Hydraulic Fractures and Natural Fractures in the KS Tight Gas Reservoir. Paper presented at EUROPEC 2015, Madrid, Spain, 1-4 June. SPE-174384-MS

Zhang, X. and Jeffrey, R. G. 2006. The Role of Friction and Secondary Flaws on Deflection and Re-Initiation of Hydraulic Fractures at Orthogonal Pre-Existing Fractures. *Geophysical Journal International* **166**(3): 1454-1465.

Zhenhua He currently is a Ph.D. candidate in the Department of Geology and Geophysics of Texas A&M University. He received the M.S. degree in petroleum engineering from Texas A&M University (College Station) and the B.S. degree in petroleum engineering from China University of Petroleum. His interests are dynamic geomechanical modeling, hydraulic fracturing, induced seismicity, source mechanisms, microseismic clouds, carbonate acidizing, reservoir simulation, data analysis and machine learning.

Benchun Duan is a professor in the Department of Geology and Geophysics of Texas A&M University. He received his Ph.D. degree in geological science from University of California, Riverside in 2006 and joined Texas A&M University as a faculty in 2007. His research interests include earthquake source physics, geomechanics, and computational seismology.